3D hierarchical *hp*-FEM applied to elasto-acoustic modelling of layered porous media

Nils-Erik Hörlin[*]

Royal Institute of Technology KTH, Aeronautical and Vehicle Engineering, MWL, 100 44 Stockholm, Sweden

Abstract

This paper presents a 3-D hierarchical (*p*-version) finite element description of the solid displacement–fluid displacement form of Biot's equation for elasto-acoustic modelling of multiple-layered isotropic porous media.

The convergence related to mesh refinement extensions for different orders of polynomial approximation is briefly discussed for a homogeneous foam. The highest computational efficiency for reasonable levels of the error in the low-frequency region was obtained for fourth-order polynomial finite element interpolations. The main focus is on coupling conditions and on the convergence of solutions to Biot's equations in cases with multiple layers having different material properties. Simulations of a two-layered porous material with low flow resistivity suggest slow convergence rate of the fluid displacement field close to the interface between the layers.

© 2004 Elsevier Ltd. All rights reserved.

1. Introduction

The increasing demand for weight and cost reductions in the design and construction of modern vehicles requires future generation of noise and vibration treatments to be more efficient as compared to the present state of the art. As a result, lightweight poroelastic materials with high internal damping have become more interesting as an alternative or a complement to traditional

---

[*]Tel.: +46 8 7909187; fax: +46 8 7906122.

   E-mail address: nisseh@kth.se (N.-E. Hörlin).

Nomenclature

Operators and functions

!	$n! = n(n-1)\ldots 1$ (faculty)
!!	$n!! = \begin{cases} n(n-2)\ldots 1, & n \text{ is odd} \\ n(n-2)\ldots 2, & n \text{ is even} \end{cases}$ (semi faculty)
int	integer part of a real number
$(v,w)_\Lambda$	L^2-inner product defined as $\int_\Lambda v\bar{w}\,d\Lambda$, where Λ is a volume or surface in $\mathbb{R}^3$ and $v,w \in L^2(\Lambda)$

Superscripts

k	finite element ordinal number
s	solid part of porous medium
f	fluid part of porous medium
$^-$	(over-line) denotes complex conjugate

Subscripts

e	sub-domain (material layer) ordinal number
i, j	component ordinal number in Cartesian coordinate system
$, i$	partial derivative with respect to the Cartesian component x_i

Variables

p	number of *hierarchical* polynomials
x_1, x_2, x_3	Cartesian spatial coordinate components
ξ_1, ξ_2, ξ_3	element local spatial coordinate components
u_i^s	displacement component in Cartesian coordinate direction i for the solid part m
u_i^f	ditto for the fluid part
v_i^s	test function for displacement component in Cartesian coordinate direction i for the solid part
v_i^f	ditto for the fluid part
$\mathbf{u}$	six-dimensional displacement component vector $\{u_1, u_2, u_3, u_4, u_5, u_6\} \equiv \{u_1^s, u_2^s, u_3^s, u_1^f, u_2^f, u_3^f\}$
$\mathbf{v}$	six-dimensional displacement component vector of test function
$\mathbf{e}$	six-dimensional component vector of error function
$\mathbf{A}()$	function which maps a finite element local coordinate system on the global coordinate system
$B(\cdot,\cdot)$	sesquilinear complex functional containing left-hand side in the weak formulation
$F(\cdot)$	antilinear complex functional containing loads and natural boundary conditions
μ	Dynamic Lamé parameter (dynamic shear modulus)
λ	Dynamic Lamé parameter at constant fluid pressure
K_b	bulk modulus of the solid frame at constant fluid pressure
K_s	bulk modulus of the material which the solid frame consists of
Q	dilatational coupling factor between the fluid phase and the solid frame
R	bulk modulus of the fluid phase at zero solid frame dilatation
b	viscous drag coefficient
ρ_{11}	corrected mass density for the solid frame
ρ_{12}	inertial coupling factor
ρ_{22}	corrected mass density of the fluid phase
ϕ	porosity
p^{pore}	homogenised fluid pore pressure
n_i	unit normal vector outward the boundary
σ_{ij}^s	Cauchy stress tensor for the porous frame
$\tilde{\sigma}_{ij}^s$	Cauchy stress tensor proposed in Ref. [9]
σ_{ij}^{s0}	Cauchy stress tensor for the porous frame in absence of fluid pressure
T_i	traction vector for the porous frame
T_i^0	structural traction vector for the porous frame
T_i^{tot}	total traction vector for the porous aggregate
ω	angular frequency

$\phi_{(l_1,l_2,l_3)}$	finite element shape function	V^0	function space of test functions with
$c_{(l_1,l_2,l_3)}$	generalised degree of freedom		domain Ω, and with those compo-
f_l	polynomial in finite element shape		nents being zero on boundaries where
	functions		essential boundary conditions exist
Ω	domain in $\mathbb{R}^3$		
V	function space of trial functions with		
	domain Ω, satisfying essential bound-		
	ary conditions		

viscoelastic layers in different configurations. In order to find optimal configurations which include poroelastic materials, accurate simulation tools are a pre-requisite.

The theory attributed to Biot [1] is used to describe poroelastic materials as coupled homogenised solid and fluid continua. Previous work on the convergence of elasto-acoustic finite element solutions for poroelastic materials has focused on homogeneous porous media, possibly coupled to a pure solid or a pure fluid media e.g. [2–4]. In Ref. [4], a three-dimensional hierarchical finite element formulation for isotropic porous media was presented. The fluid displacements and the solid displacements were used as dependent variables, as in the original formulation by Biot. The *p*-convergence was studied for a parallelepiped-shaped geometry with realistic material parameters representing a polyurethane foam material. A general observation was that *p*-enrichment gave fast convergence in comparison with mesh refinements of linear and quadratic elements. However, only one single element was considered for the *p*-extensions.

As an extension of previous work by the same author, this paper briefly discusses mesh refinements of hierarchical elements, together with boundary conditions and coupling conditions of porous sub-domains having different material properties. In Section 2, a weak form of Biot's equation for a layered porous material will be stated in a general way and an alternative equivalent way of writing the boundary integral is proposed. Details of situation-specific coupling conditions and boundary conditions will be covered in Sections 3 and 4. In Section 5, the hierarchical finite element basis and its implementation are briefly described. In Section 6, the *hp*-convergence, here defined as the mesh refinement convergence for different values of *p* [5], is studied for the same case (geometry, material and loading) as in Ref. [4]. To illustrate the behaviour of finite element solutions for a layered media, a numerical example of a two-layered porous material is presented in Section 7. The material properties in the first layer, are identical to the previous example. In the second layer, the volume porosity is taken to be different and as a result the fluid displacement will be discontinuous over the layer interface. It is shown that slow convergence exclusively for the fluid displacement occurs close to the layer interface in both layers in this example. This slow convergence behaviour decreases as the flow resistivity is taken to be increased. Both in the single-layer example and the two-layer example, it is shown that higher-order polynomials are needed to accurately describe the displacement fields with an acceptable computational efficiency.

2. Weak formulation of Biot's equations

Consider a three-dimensional regular open domain $\Omega \subset \mathbb{R}^3$ enclosed by its boundary Γ. Ω is considered to be composed of geometrically disjoint sub-domains Ω_e, $e = 1, 2, \ldots, N^e$. These

sub-domains represent layers with different material properties. It is also assumed that these properties are uniform within each sub-domain. The boundaries Γ_e which enclose Ω_e may be divided into two parts: on one hand the joint boundaries of mutually adjacent sub-domains and on the other hand, the disjoint part. The former part are coupling interfaces on which *coupling conditions* have to be imposed. These are dependent on the way different material layers are attached to each other, and are described in some detail in Section 4. However, common to all coupling conditions the conservation of fluid flux

$$\phi_1 u_i^{f1} n_i^1 + (1 - \phi_1) u_i^{s1} n_i^1 = \phi_2 u_i^{f2} n_i^1 + (1 - \phi_2) u_i^{s2} n_i^1 \tag{1}$$

and also Newtons third law of action and reaction, i.e., traction vector symmetry

$$T_i^{\text{tot1}} + T_i^{\text{tot2}} = 0 \tag{2}$$

must always be satisfied. (T_i^{tot1} and T_i^{tot2} are the total traction vectors of two adjacent sub-domains with labels 1 and 2.) The latter part defines the outer boundary Γ where the *boundary conditions* are imposed. Different kinds of boundary conditions are discussed in Section 3. If material isotropy, time harmonic motion and small displacements are assumed, a displacement form of Biot's equations may be written as [4]

$$\mu u_{i,jj}^s + (\lambda + \mu) u_{j,ji}^s + (\omega^2 \rho_{11} - i\omega b) u_i^s + Q u_{j,ji}^f + (\omega^2 \rho_{12} + i\omega b) u_i^f = 0, \tag{3a}$$

$$Q u_{j,ji}^s + (\omega^2 \rho_{12} + i\omega b) u_i^s + R u_{j,ji}^f + (\omega^2 \rho_{22} - i\omega b) u_i^f = 0. \tag{3b}$$

All derivatives are with respect to the spatial coordinates x_i, $i = 1, 2, 3$ in a global Cartesian coordinate system. The material parameters λ, μ, Q, R, b, K_b, K_s and K_f should be considered as complex-valued and dependent of the angular frequency ω. The derivation of the material parameters are described in Refs. [6–8].

Eqs. (3a) and (3b) may be multiplied by suitable test functions and then integrated by parts. Then a weak form of Biot's equations in each sub-domain may be written as [4]

$$\begin{aligned}&\text{Find } \mathbf{u} \in V_e \text{ such that}\\&B_e(\mathbf{u}, \mathbf{v}) = F_e(\mathbf{v}) \quad \forall \mathbf{v} \in V_e^0,\end{aligned} \tag{4}$$

where

$$\begin{aligned} B_e(\mathbf{u}, \mathbf{v}) &\overset{\text{def}}{=} \mu(u_{i,j}^s, v_{i,j}^s)_{\Omega_e} + \mu(u_{j,i}^s, v_{i,j}^s)_{\Omega_e} + (\lambda + Q^2/R)(u_{j,j}^s, v_{i,i}^s)_{\Omega_e} \\ &\quad - \omega^2 \rho_{11}(u_i^s, v_i^s)_{\Omega_e} + i\omega b(u_i^s, v_i^s)_{\Omega_e} \\ &\quad + Q(u_{j,j}^f, v_{i,i}^s)_{\Omega_e} - \omega^2 \rho_{12}(u_i^f, v_i^s)_{\Omega_e} - i\omega b(u_i^f, v_i^s)_{\Omega_e} \\ &\quad + Q(u_{j,j}^s, v_{i,i}^f)_{\Omega_e} - \omega^2 \rho_{12}(u_i^s, v_i^f)_{\Omega_e} - i\omega b(u_i^s, v_i^f)_{\Omega_e} \\ &\quad + R(u_{j,j}^f, v_{i,i}^f)_{\Omega_e} - \omega^2 \rho_{22}(u_i^f, v_i^f)_{\Omega_e} + i\omega b(u_i^f, v_i^f)_{\Omega_e} \end{aligned} \tag{5a}$$

and

$$F_e(\mathbf{v}) \overset{\text{def}}{=} (\tilde{\sigma}_{ij}^s n_j, v_i^s)_{\Gamma_e^s} + (Q/R)(-\phi p^{\text{pore}} n_i^e, v_i^s)_{\Gamma_e^{sf}} + (-\phi p^{\text{pore}} n_i^e, v_i^f)_{\Gamma_e^f}, \tag{5b}$$

n_i^e pointing outwards from the sub-domain. See Nomenclature for the definition of L^2-inner products $(\cdot, \cdot)_\Lambda$. Expressions (5a) and (5b) were derived in detail in Ref. [4] and will not be repeated here. In the whole domain, Ω, the weak formulation is written as

$$\text{Find } \mathbf{u} \in V :$$
$$B(\mathbf{u}, \mathbf{v}) = F(\mathbf{v}) \quad \forall \mathbf{v} \in V^0, \tag{6}$$

where $B(\mathbf{u}, \mathbf{v}) = \sum_{e=1}^{Ne} B_e(\mathbf{u}, \mathbf{v})$. It may be shown that, in order to satisfy the Eqs. (1) and (2), boundary integrals from mutually adjacent sub-domains must cancel out. Hence $F(\mathbf{v})$ is identified as $F(\mathbf{v}) = \sum_{e=1}^{Ne} F_e(\mathbf{v})$. V is defined as a subset of the Cartesian product of all V_e such that the kinematic boundary conditions and the kinematic couplings between the sub-domains are satisfied. V^0 is similarly defined, but with the homogeneous corresponding kinematic boundary conditions satisfied.

The stress tensor $\tilde{\sigma}_{ij}^s$ in Eq. (5b), proposed by Atalla in Ref. [9], is defined as

$$\tilde{\sigma}_{ij}^s \stackrel{\text{def}}{=} \mu(u_{i,j}^s + u_{j,i}^s) + \lambda u_{k,k}^s \delta_{ij}. \tag{7}$$

The frame stress is then written as (cf. Ref. [6])

$$\sigma_{ij}^s = \tilde{\sigma}_{ij}^s + (Q^2/R)u_{k,k}^s \delta_{ij} + Q u_{k,k}^f \delta_{ij} \tag{8}$$

and the pore pressure as [6]

$$-\phi p^{\text{pore}} = Q u_{k,k}^s + R u_{k,k}^f. \tag{9}$$

If Eq. (9) is inserted in Eq. (8), then $u_{k,k}^f$ is eliminated and the stress in the frame is then written as [9]

$$\sigma_{ij}^s = \tilde{\sigma}_{ij}^s + (Q/R)(-\phi p^{\text{pore}}). \tag{10}$$

Unlike σ_{ij}^s, $\tilde{\sigma}_{ij}^s$ is not explicitly dependent of u_i^f. However, on a boundary where the frame is only in contact with a surrounding fluid with the pressure $p = p^{\text{pore}}$ (see Eq. (29)), not only σ_{ij}^s but also $\tilde{\sigma}_{ij}^s$ is non-zero since according to Ref. [6] in such a case,

$$u_{j,j}^s = -p^{\text{pore}}/K_s, \tag{11}$$

where K_s is the bulk modulus for the solid material from which the frame is made. If Eq. (11) is inserted in Eq. (7), the stress tensor $\tilde{\sigma}_{ij}^s$ is obviously non-zero.

To simplify the formulation of certain boundary conditions, it might be advantageous to seek an alternative division of the frame stress into parts of pure structural origin σ^{s0} and pure fluid pressure origin σ_{ij}^{sp}, i.e.,

$$\sigma_{ij}^s = \sigma_{ij}^{s0} + \sigma_{ij}^{sp}. \tag{12}$$

Such division allows pure structural load and pure fluid pressure load to be specified independently in a convenient way. The frame dilatation $u_{j,j}^s$ is likewise decomposed into

$$u_{j,j}^s = u_{j,j}^{s0} + u_{j,j}^{sp}, \tag{13}$$

where $u_{j,j}^{s0}$ is the frame dilatation induced by a pure structural (transparent) load in the absence of fluid pressure. The corresponding structurally induced frame stress is

$$\sigma_{ij}^{s0} = \mu(u_{i,j}^{s0} + u_{j,i}^{s0}) + \lambda u_{k,k}^{s0}\delta_{ij}. \tag{14}$$

In the other part, $u_{j,j}^{sp}$ is the frame dilatation induced by the pore pressure in the absence of any structurally induced load and is given by [6]

$$u_{j,j}^{sp} = -p/K_s, \tag{15}$$

as in Eq. (11). Inserting Eq. (7) in Eq. (10), the stress–strain relation for the corresponding pore pressure-induced frame stress may be written as

$$\sigma_{ij}^{sp} = (K_b u_{k,k}^{sp} + (Q/R)(-\phi p^{\text{pore}}))\delta_{ij}, \tag{16}$$

since no shear is involved in this case; $K_b = \lambda + \frac{2}{3}\mu$ is the bulk modulus for the porous frame in the absence of pore pressure. According to Ref. [6], this stress is related to the applied pore pressure by

$$\sigma_{ij}^{sp} = -(1 - \phi)p^{\text{pore}}\delta_{ij}. \tag{17}$$

From the expressions of Q and R in Ref. [6], $(Q/R)\phi$ is derived as

$$(Q/R)\phi = 1 - \phi - K_b/K_s. \tag{18}$$

If Eq. (18) along with Eq. (15) are inserted into Eq. (16), Eq. (17) is obtained as expected. The total stress of the porous aggregate $\sigma_{ij}^{\text{tot}} \stackrel{\text{def}}{=} \sigma_{ij}^s + (-\phi p^{\text{pore}})\delta_{ij}$ is in this particular case simply equal to $-p^{\text{pore}}\delta_{ij}$ as expected, and in general $\sigma_{ij}^{\text{tot}} = \sigma_{ij}^{s0} - p^{\text{pore}}\delta_{ij}$. If Eq. (17), is inserted into Eq. (12), the frame stress may be written as the superposition of a pure structural part and a pure pore pressure part contribution, i.e.,

$$\sigma_{ij}^s = \sigma^{s0} - (1 - \phi)p^{\text{pore}}\delta_{ij}. \tag{19}$$

This decomposition simplifies the specification of the natural boundary conditions in Section 3. Finally, Eq. (5b) may now be written as

$$F_e(\mathbf{v}) \stackrel{\text{def}}{=} (T_i^0, v_i^s)_{\Gamma_e^s} + (1 - \phi)(-p^{\text{pore}}n_i^e, v_i^s)_{\Gamma_e^{sf}} + (-\phi p^{\text{pore}}n_i^e, v_i^f)_{\Gamma_e^f}, \tag{20}$$

where $T_i^0 \stackrel{\text{def}}{=} \sigma_{ij}^{s0}n_j$ is the structural traction vector.

The coupling conditions between adjacent sub-domains will be discussed in more detail in Section 4. However, to arrive at these, it is useful to review some combinations of boundary conditions first.

3. Boundary conditions

A porous boundary may, referring to Biot's original work, be classified as *jacketed* or *unjacketed*.

Jacketed means that the normal component of the solid displacement and the normal component of the fluid displacement are assumed to be equal, i.e.,

$$u_i^f n_i = u_i^s n_i. \tag{21}$$

A jacket may be regarded as a thin impervious membrane covering, the boundary. For this kind of covering, only the pure Dirichlet condition or the pure Neumann conditions in the normal direction for both the frame and the fluid may be specified at the boundary. This is clear from the dependence between the normal displacement components of the frame and the fluid described by Eq. (21).

Unjacketed means, on the other hand, that these normal components are not mutually constrained and thus that also *mixed* Neumann and Dirichlet conditions are allowed to be specified for the fluid and the frame. For the Dirichlet conditions, the normal component of frame displacements or the normal component of the fluid displacement is prescribed. However, prescription of the fluid displacement on an unjacketed boundary are merely of formal character. A more physical boundary condition is an *injection condition*, where the amount of fluid which enters the porous aggregate is prescribed. This may be written as a prescription of the normal component of the total displacement, i.e.,

$$(1 - \phi)u_i^s n_i + \phi u^f n_i = u_\Gamma^{\text{tot}}. \tag{22}$$

These boundary conditions may be combined with Dirichlet or Neumann condition on the frame (see below). In the former case, this is equivalent to the pure Dirichlet condition, previously mentioned, but in the latter case the injection condition must be imposed as a linear constraint equation given by Eq. (22), where in this case $u^f n_i$ must be constrained (eliminated).

For the Neumann condition, the normal component of the structural traction vector $T_i^0 n_i$ is prescribed for the frame and the ambient pressure p is prescribed for the fluid. It should be noted that the normal component of the frame stress traction vector $T_i n_i = n_i \sigma_{ij}^s n_j$ is only known a priori in the case of the pure Neumann condition from Eq. (19), since it includes both the structural traction vector and the ambient pressure.

In case of the pure Neumann condition for a jacketed boundary, the normal component of the structural traction vector and the pore pressure is not prescribed separately, but only the normal component of the total stress traction vector

$$T_i^{\text{tot}} n_i = n_i \sigma_{ij}^s n_j - \phi p \tag{23}$$

is known a priori and may be prescribed. This is consistent with Eq. (20) since the test functions for the solid and the fluid on the boundary are constrained according to Eq. (21).

Note that in the above discussion only conditions normal to the boundary are considered. The tangential components of the structural displacement $u_i^s - u_j^s n_j n_i$ (for the Dirichlet condition) or the tangential components of the structural traction vector $T_i^0 - T_j^0 n_j n_i$ (for the Neumann condition) are not involved in this classification and such boundary conditions are here treated

separately and independently of the normal conditions, regardless of whether the boundary is jacketed or not.

4. Coupling conditions

In the following, different types of coupling conditions between a porous medium and another porous, pure solid or pure fluid medium are described. Superscripts 1 and 2 are labels of the adjacent sub-domains, here also referred to as *layers*. The most fundamental conditions that must be satisfied are the conservation of fluid flux (Eq. (1)) and the symmetry of the total traction vectors (Eq. (2)).

4.1. Kinematic coupling conditions

If the adjacent media are structurally attached, then also

$$u_i^{s1} = u_i^s = u_i^{s2}. \tag{24}$$

This is referred to as *bonded conditions* and reduces Eq. (21) to

$$\phi_1 u_i^{f1} n_i^1 = \phi_2 u_i^{f2} n_i^1 + (\phi_1 - \phi_2) u_i^s n_i^1. \tag{25}$$

As can be seen, the normal component of the fluid displacement is discontinuous over the coupling interface if $\phi_1 \neq \phi_2$.

If also at least one of the layers is jacketed (the other layer will in such a case be covered by the same jacket), then by Eq. (21), Eq. (25) is further reduced to

$$u_i^{f1} n_i^1 = u_i^s n_i^1 = u_i^{f2} n_i^1. \tag{26}$$

Now also the normal component of the fluid displacement is continuous over the coupling interface.

On the other hand, consider the situation where the layers are not in structural contact but in between the layers there is a fluid-filled gap, much smaller than the wave length. This so-called *unbonded* coupling [10] is imposed by only assuming conservation of fluid flux (Eq. (1)) if both layers are unjacketed. If one of the layers is jacketed, say layer 1, then Eq. (1) is reduced by Eq. (21) to

$$u_i^{f1} n_i^1 = u_i^{s1} n_i^1 = \phi_2 u_i^{f2} n_i^1 + (1 - \phi_2) u_i^{s2} n_i^1. \tag{27}$$

For the unbonded case, both the solid and the fluid displacements are discontinuous over the coupling interface.

As a general remark, it may be noted that the tangential part of the fluid displacement is never coupled and is hence in general discontinuous over a coupling interface (even if $\phi_1 = \phi_2$). This is a consequence of the nature of the homogenised fluid, which is assumed as inviscid within the Biot theory. (The viscous effects of the real fluid on the pore scale are homogenised and is included by the Biot parameter b in Eqs. (3a) and (3b).) However, if two unjacketed adjacent porous layers, having identical material properties, are bonded, they may obviously be treated as one layer. Thus, the tangential part of the fluid displacement may, in such a case, be assumed to be

continuous, i.e.,

$$u_i^{f1} - u_j^{f1} n_j^1 n_i^1 = u_i^{f2} - u_j^{f2} n_j^1 n_i^1. \tag{28}$$

Of course, this assumption is based on the underlying requirement that the loads are sufficiently regular.

4.2. Dynamic coupling conditions

In addition to the symmetry of the total traction vectors, the following may be observed. If both adjacent layers are unjacketed, then the pore pressure is continuous, i.e.,

$$p^{\text{pore1}} = p^{\text{pore2}}, \tag{29}$$

since the pores are communicating over the interface, otherwise not. This also implies symmetry of the structural traction vectors, i.e.,

$$T_i^{01} + T_i^{02} = 0. \tag{30}$$

If the adjacent layers are unbonded, these structural traction vectors are both zero. Then, also the tangential part of the total traction vectors is zero, i.e.,

$$(T_i^{\text{tot1}} - T_j^{\text{tot1}} n_j^1 n_i^1) = (T_i^{\text{tot2}} - T_j^{\text{tot2}} n_j^1 n_i^1) = 0, \tag{31}$$

which may be shown to be equivalent to

$$(T_i^{01} - T_j^{01} n_j^1 n_i^1) = (T_i^{02} - T_j^{02} n_j^2 n_i^2) = 0. \tag{32}$$

Consider the boundary integrals $F(\mathbf{v})^1$ and $F(\mathbf{v})^2$ defined over $\mathbf{x} \in \Gamma_{12}$, where Γ_{12} is the interface between two layers. If any of the kinematic coupling conditions described in this section is imposed on the test functions, and also considering the corresponding dynamic coupling conditions, then it is evident that

$$F(\mathbf{v})^1 + F(\mathbf{v})^2 = 0. \tag{33}$$

It may be noted that, in the context of coupling conditions for porous layers, the coupling condition to a pure fluid is identical to the unbonded coupling to an unjacketed porous material with $\phi = 1$. Similarly, the coupling condition to a pure solid is identified as the coupling to a jacketed porous medium with $\phi = 0$.

Finally, it may be concluded that in those coupling situations, previously described, where discontinuities of the displacements occur, these kinematic coupling equations must be imposed as additional constraint equations. This complexity of implementation does not occur in fluid pore pressure formulations e.g. Ref. [9], since the fluid pore pressure is continuous over material discontinuities if the coupling interfaces are unjacketed. If an interface is jacketed, however, the pore pressure is discontinuous.

5. Hierarchical finite element basis for a hexahedral finite element

Consider a cube-shaped finite element with a Cartesian local coordinate system (ξ_1, ξ_2, ξ_3). This coordinate system has a one-to-one correspondence to the Cartesian global coordinate system by $(x_1, x_2, x_3) = \mathbf{A}_k(\xi_1, \xi_2, \xi_3)^k$, where $\mathbf{A}_k$ is a bijective mapping which defines the actual geometry (possibly curvilinear, but with hexahedral topology) of the kth finite element. The local coordinates are hereafter tagged with a superscript k to denote the unique relation to the global coordinate system. Let any of the six displacement components of $\mathbf{u}$ be approximated to

$$u_i^k(\xi_1, \xi_2, \xi_3)^k = \sum_{l_1=1}^{p_1+2} \sum_{l_2=1}^{p_2+2} \sum_{l_3=1}^{p_3+2} c_{i(l_1,l_2,l_3)}^k \phi_{(l_1,l_2,l_3)}(\xi_1, \xi_2, \xi_3)^k, \tag{34}$$

and choose as test functions

$$\mathbf{v}_{j(m_1,m_2,m_3)}^k = \boldsymbol{\delta}_j \phi_{(m_1,m_2,m_3)}(\xi_1, \xi_2, \xi_3)^k \quad \forall k, j, m_1, m_2, m_3, \tag{35}$$

where the six-dimensional vector $\boldsymbol{\delta}_i$ is defined as

$$\boldsymbol{\delta}_i = \{\delta_{ik}\}_{k=1}^6. \tag{36}$$

The coefficients $c_{i(l_1,l_2,l_3)}^k$ are called finite element degrees of freedoms (dofs). Each basis function $\phi_{(l_1,l_2,l_3)}(\xi_1, \xi_2, \xi_3)^k$ (or so-called shape function) is composed of a product of three polynomials [4] with local support over the cube, i.e.,

$$\phi_{(l_1,l_2,l_3)}(\xi_1, \xi_2, \xi_3)^k \stackrel{\text{def}}{=} \begin{cases} f_{l_1}(\xi_1) f_{l_2}(\xi_2) f_{l_3}(\xi_3), & (\xi_1, \xi_2, \xi_3)^k \in [-1, 1], \\ \text{zero} & \text{elsewhere.} \end{cases} \tag{37}$$

These polynomials are here defined as [11,4]

$$f_l(\chi) \stackrel{\text{def}}{=} \begin{cases} \frac{1}{2}(1 - \chi), & l = 1, \\ \frac{1}{2}(1 + \chi), & l = 2, \\ \sum_{s=0}^{\text{int}(l/2)} \dfrac{(-1)^s (2l - 2s - 5)!!}{2^s s! (l - 2s - 1)!} \chi^{l-2s-1}, & l \geqslant 3. \end{cases} \tag{38}$$

The polynomials for $l \leqslant 3$ are referred to as hierarchical polynomials and p is the number of hierarchical polynomials used in the basis; $p + 1$ denotes the order of the polynomial basis used. It may be shown that each of those shape functions, previously defined, which is non-zero at a finite element boundary, is associated with a particular corner, edge, or surface. The corresponding dof is given the same association.

Now, define a mesh of elements on each sub-domain and insert Eqs. (34) and (35) into Eq. (4). Then, for any k,

$$\mathbf{K}^k \mathbf{c}^k = \mathbf{f}^k \tag{39}$$

is obtained, where $\mathbf{c}^k = \{c_{i(l_1,l_2,l_3)}^k\}$. The elements of the dynamic finite element stiffness matrix $\mathbf{K}^k$ and the finite element load vector $\mathbf{f}^k$ are given by

$$K_{j(m_1,m_2,m_3),i(l_1,l_2,l_3)}^k = B_e(\phi_{(l_1,l_2,l_3)}(\xi_1, \xi_2, \xi_3)^k \boldsymbol{\delta}_i, \phi_{(m_1,m_2,m_3)}(\xi_1, \xi_2, \xi_3)^k \boldsymbol{\delta}_j) \tag{40}$$

and

$$f^k_{j(m_1,m_2,m_3)} = F_e(\phi_{(m_1,m_2,m_3)}(\xi_1,\xi_2,\xi_3)^k \mathbf{\delta}_j). \tag{41}$$

To evaluate the integrals in Eqs. (40) and (41), the mapping $\mathbf{A}^k$ is needed to transform the integrals into the $(\xi_1,\xi_2,\xi_3)^k$-coordinate system.

Kinematic coupling conditions on sub-domain coupling interfaces are introduced on the element level as linear constraint equations, which transforms these finite element stiffness matrices into constrained matrices

$$\mathbf{K}^k_c \mathbf{c}^k_c = \mathbf{f}^k_c. \tag{42}$$

In this transformation, some dofs are eliminated and some dofs from the adjacent sub-domain are temporarily added. This procedure is described in detail in Ref. [12]. The remaining coupling dofs are constrained to be equal to the corresponding dofs of adjacent finite elements (associated with the same geometrical entity). (Here it is assumed that adjacent meshes are compatible with respect to finite element geometry and that the same order of approximation is used for the displacements on adjacent surfaces.) This further reduces the number of independent dofs and couples the element equations into a global system which may be written as

$$\mathbf{Kc} = \mathbf{f}. \tag{43}$$

This is a matrix representation of a finite-dimensional subspace version of Eq. (6). Finally, equations from prescribed dofs are removed and the contributions of these prescribed dofs in other equations are included in the right-hand side and are interpreted as reaction forces.

6. Numerical example of single-homogeneous polyurethane foam

6.1. Description of the numerical example

A parallelepiped-shaped domain with dimensions $0.2\,\text{m} \times 0.3\text{m} \times 0.5\text{m}$ in 1-, 2- and 3-direction, respectively, is considered, with the non-homogeneous Neumann condition imposed on the face, which is pointing in the negative 3-direction. On this face, the structural traction vector is prescribed to $(0,0,1)$, i.e., a unity normal traction vector in the positive 3-direction. On all other boundaries, the homogeneous Neumann condition is imposed. The material parameters represent a polyurethane foam with open cell structure and are given in Table 1. The derivation of the Biot parameters Q, R, b, ρ_{11}, ρ_{12} and ρ_{22} from the material parameters is described in Refs. [4,6,10] and is not repeated here. The dynamic complex-valued Lamé moduli μ, λ, which include internal material damping in the frame, are derived from an augmented Hooke's law by Dovstam, described in Refs. [4,7,8].

In the simulations performed, the frequencies 100 and 200 Hz are considered. These frequencies were chosen as two samples in the low-frequency region, exhibiting varying degrees of fluid–frame coupling and difference in wave length. Some properties of the three Biot waves are given in Fig. 1 as functions of the frequency. The decoupling frequency of the compressional waves is about 70 Hz. Hence, the compressional waves will here be referred to as frame borne, and air borne, respectively. At both 100 and 200 Hz, the air-borne wave is the most damped one and the shear

Table 1
Material properties for a polyurethane foam

Static Young's modulus	70.0×10^3 Pa
Static Poisson's ratio	0.39
Porous material density	22.1 kg/m^3
Porosity	0.98
Fluid density	1.204 kg/m^3
Fluid dynamic viscosity	1.84×10^{-5}
Fluid ratio of specific heats	1.4
Prandtl number	0.71
Viscous characteristic length	1.1×10^{-4} m
Thermal characteristic length	7.42×10^{-4} m
Static flow resistivity	3.75×10^3 kg/m^3 s
Tortuosity	1.17
Thermal form factor	0.25
Gas constant (for air)	286.7 m^2/s^2 K
Absolute temperature	293.15 K

Augmented Hooke's law parameters [7,8]: $\alpha_1 = 1.0$, $\beta_1 = 3.1416$, $\varphi_1 = 71.95$, $\mu_1 = 71.30$; $\alpha_2 = 1.0$, $\beta_2 = 6.28 \times 10^4$, $\varphi_2 = 0$, $\mu_2 = 396.74$.

wave is least damped one. At 200 Hz, the damping of the frame-borne wave is only slightly lower than that of the shear wave. This implies most likely in combination with the nature of the excitation that the displacement field should be dominated by rotational waves and also possibly the compressional frame-borne waves. For the sake of simplicity and guaranteed convergence, the simulations are also limited to isotropic and homogeneous (uniform) p-enrichments and mesh refinements. That is, $p_1 = p_2 = p_3 = p$ and the number of elements are the same in each coordinate direction. In the following, this latter mesh size parameter is denoted by k. Hence, the total number of elements is k^3. Higher computational efficiency may be obtained by using non-uniform meshes and anisotropic and non-uniform p-enrichments. This issue of adaptive hp-strategies is, however, beyond the scope of the present work.

The quality of the solutions is evaluated in a relative error measure $\mathscr{E}_{\mathrm{rel}} \stackrel{\mathrm{def}}{=} |F(\bar{\mathbf{e}})|^{1/2}/|F(\bar{\mathbf{u}})|^{1/2}$ proposed in Ref. [4]. Since the exact solution is not available, this measure is approximated to $\mathscr{E}_{\mathrm{rel}} \approx |(F(\bar{\mathbf{u}}_{\mathrm{ref}}) - F(\bar{\mathbf{u}}_{\mathrm{FE}}))/F(\bar{\mathbf{u}}_{\mathrm{ref}})|^{\frac{1}{2}}$, where the reference solution $\mathbf{u}_{\mathrm{ref}}$ here is the solution for $p = 16, k = 1$. This is also discussed in Ref. [4]. A relative error less than 10^{-2} corresponds to perfect match in eye-scope measure of a deflection shape.

Convergence is measured in terms of the number of dofs, as well as in terms of solution time. In the present calculation, the equation solver, used is a front solver, where fully populated element stiffness matrices are processed. As a result, despite the element stiffness matrices getting increasingly sparse for higher values of p for parallelepiped-shaped elements (due to the orthogonality properties of the hierarchical polynomials), the same computational time is obtained as for curve-shaped elements (which, in general, have fully populated element stiffness matrices). This is a conservative approach from the point of view of estimating the computational efficiency (and would be alleviated in high-performance computing applications). Obviously, the
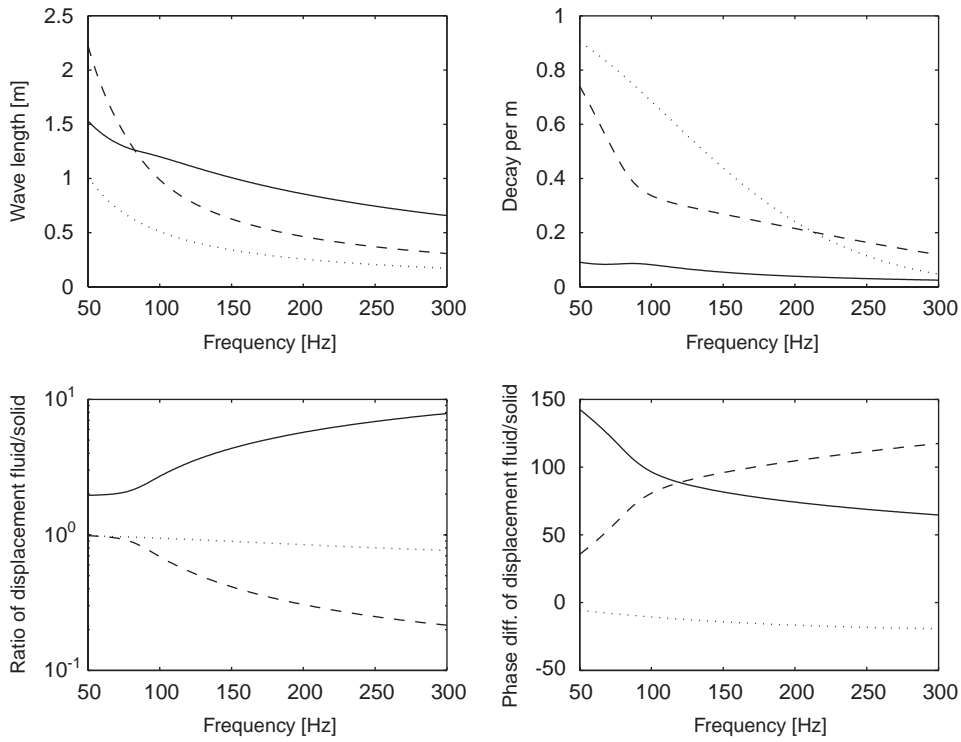
Fig. 1. Wave properties for the air-borne compression wave (solid line), the frame-borne compression wave (dashed line) and the shear wave (dotted line) versus the frequency. (The decay rate is close to one for a lowly damped wave.)

high sparsity of element stiffness matrices strongly reduces the computational cost if an equation solver designed for sparse matrices is used. E.g., simulations in Ref. [4] showed that the computation time per dof for p-enrichment extensions of a single parallelepiped-shaped element increased with approximately the same rate as for mesh refinement extension of low-order p. However, the additional time for the numerical integration, which is needed for curve-shaped elements, is still not taken into account.

6.2. Result and discussion

To survey the behaviour of the solutions, deformed plots of displacement fields are shown in Figs. 2 and 3. At both frequencies, the solid displacement and the fluid displacement have fairly similar behaviours. As can be seen from these figures, the displacement fields are quite "three-dimensional" in the sense that the displacements perpendicular to the imposed traction vector load are significant as compared to the displacements parallel to the load.

In Figs. 4 and 7, the hp-convergence for uniform meshes is shown versus the number of real-valued dofs. (Real-valued dofs are used since the complex-valued equation system obtained from the Biot's equation must be rewritten into a real-valued indefinite equation system with double size, in order to be solved by a real-valued equation solver.) In these simulations, the asymptotic behaviour of the convergence [13] seems only to be captured for the lower-order elements $p = 0$,
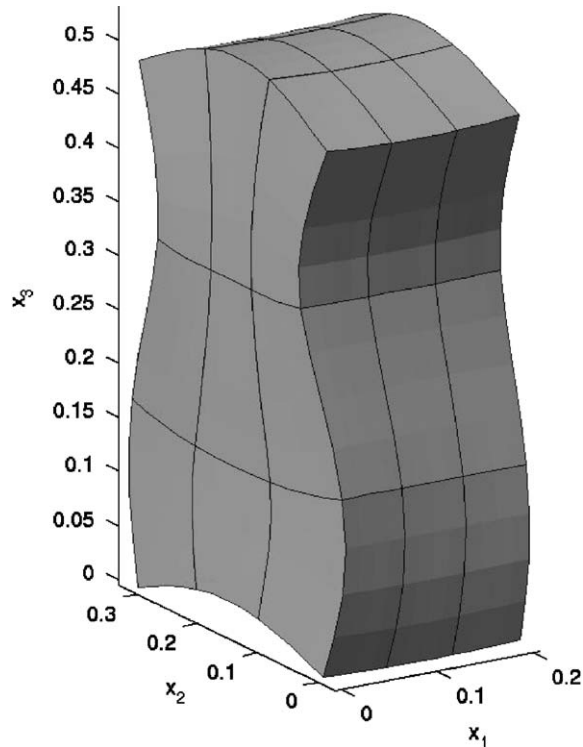
Fig. 2. Deformation plot of the imaginary part of the fluid displacement at 100 Hz ($p = 3, k = 3$, magnification factor of deformations: 20,000).

$p = 1$ and possibly for $p = 2$. Irregularities of the convergence for higher p in the pre-asymptotic range have been observed in Ref. [4] for this problem and in Ref. [5] for one-dimensional Helmholtz equation. This is due to the even–odd effect of the chosen polynomial basis, i.e. every second extension adds only odd polynomials and vice versa.

The computational efficiency of different p is not as obvious as the convergence versus the number of dofs. As illustrated in Figs. 5 and 8, the computation time not only depends on the number of dofs. When using a frontal solver, the front-width of the equation system is a decisive factor. (This is in analogy with the influence of the bandwidth for a skyline solver.) The computation time may approximately be estimated to be proportional to the square of the average front-width times the number of elements. For instance, in the case of one element with high order of p, the number of operations is proportional to the cube of the number of real dofs, while in the case of low order of p and many elements stacked in one direction, the number of operations is proportional to the square of the number of dofs in an element times the number of elements. For a dense, lower-order mesh, the number of operations per dof is lower than for a sparse, higher-order mesh with the same number of dofs. Despite these favourable numbers, the extensions for $p = 0$ and 1 are computationally inefficient due to their slow convergence, as can be seen in Figs. 4, 7, 5 and 8. Figs. 6 and 9 show the magnitude of the displacement in the 3-direction along straight lines parallel to the 3-direction. These samples of displacements are fairly representative
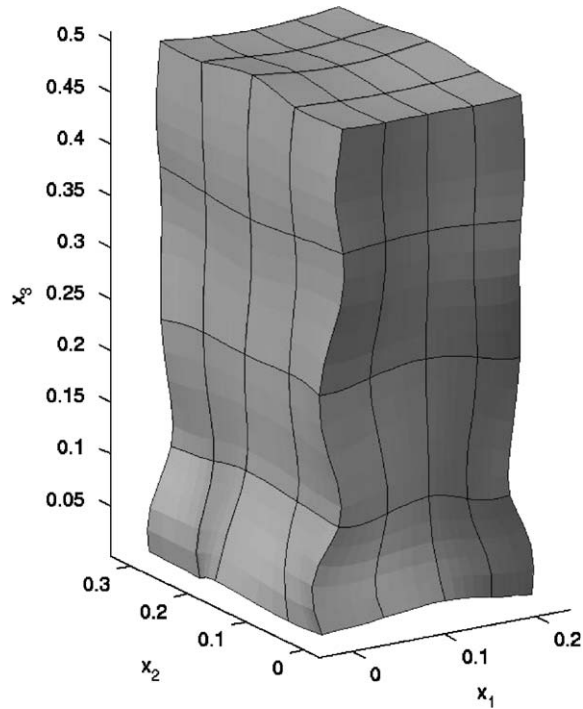
Fig. 3. Deformation plot of the imaginary part of the solid displacement at 200 Hz ($p = 4, k = 4$, magnification factor of deformations: 40,000). Note that the deformation is symmetric with respect to the 1–3-plane and the 2–3-plane, despite the presence of an apparent non-symmetric appearance as an effect of the projection of a three-dimensional deformation onto a two-dimensional plot.
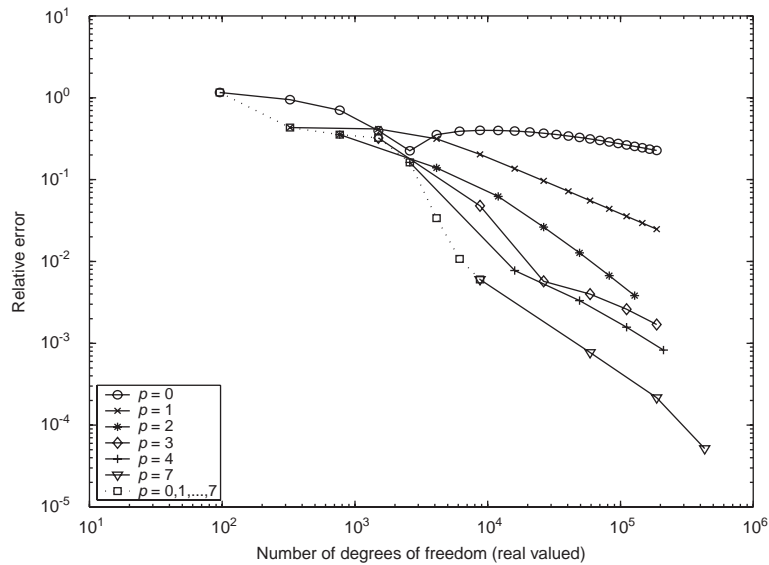

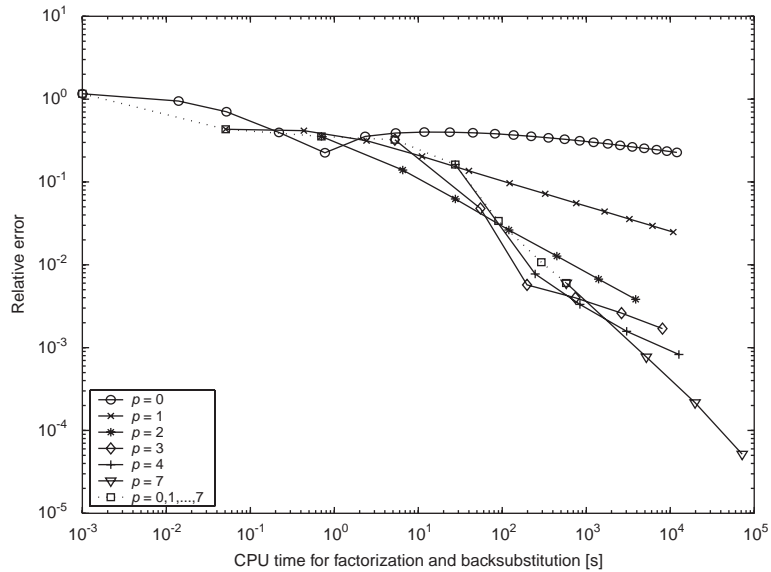Fig. 4. Relative error for mesh refinement extensions versus number of real-valued dofs at 100 Hz.

Fig. 5. Relative error for mesh refinement extensions versus CPU time at 100 Hz.

of the quality of the solutions from extensions of different p and k, having approximately the same computational time. Here, the linear element ($p = 0$) clearly distinguishes itself as having bad performance. At two 200 Hz, the linear solution in Fig. 9 seems to have a significant dispersion error.

Furthermore, a cut-on limit can also be seen in Figs. 4, 7, 5 and 8, before which the extensions for $p \geqslant 1$ all have similar convergence rates. This cut-on limit is shifted to the right and is more distinct for 200 Hz than 100 Hz. Similar cut-on behaviour was also observed in Refs. [4,5] and the limit is most likely related to the wave length. It can also be concluded that there is not necessarily much to gain, from a computational effort point of view, by increasing the value of p above $p = 3$. In fact, if the required relative error is of the order 10^{-2}, then $p = 3$ gives higher accuracy than $p = 4$, with less computational effort. These results may give a guideline for choosing the value of p. It should be noted that, nevertheless, as evident in Figs. 5 and 8, asymptotically as the number of dofs increases towards infinity, the highest computational efficiency is obtained from the mesh refinement extension of the highest order of p. This has previously been shown for acoustical scattering problems [5] (Figs. 7–9).

7. Numerical example using a two-layered material

7.1. Description of the numerical example

Consider a two-layered material each with 1 cm thickness in the stacking direction. The cross-sectional dimensions are 1 dm × 1 dm. See Fig. 10. The material properties for the two layers differs only in the volume porosity ϕ. The two layers are hereafter denoted as layers 1 and 2. The
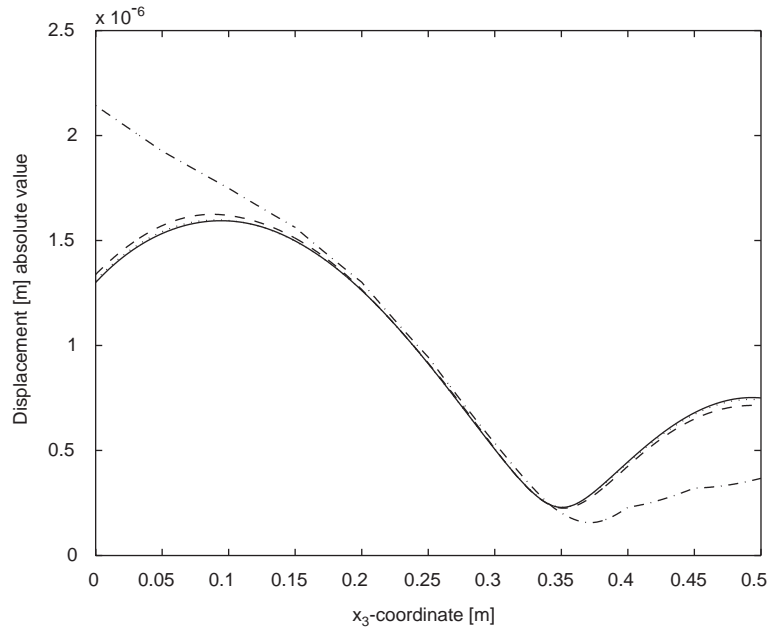
Fig. 6. u_3^f at 100 Hz: $x_1 = 0.04$ m, $x_2 = 0.24$ m. $p = 0$, $k = 10$ (dashed–dotted line); $p = 1$, $k = 5$ (dashed line); $p = 2$, $k = 3$ (dotted line); reference solution (solid line).
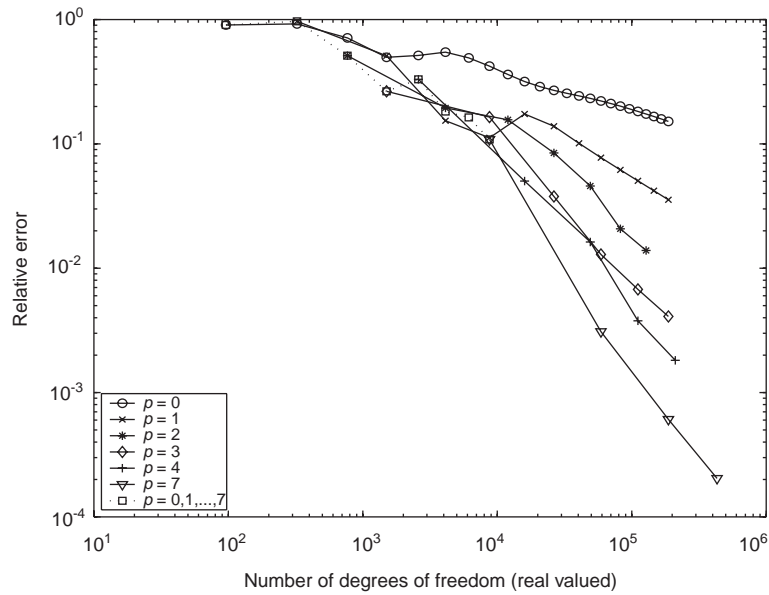

Fig. 7. Relative error for mesh refinement extensions versus number of real-valued dofs at 200 Hz.
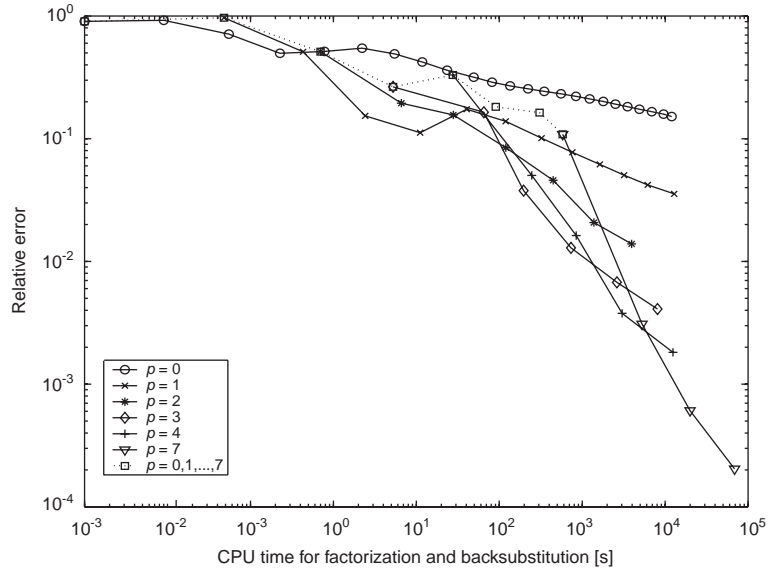
Fig. 8. Relative error for mesh refinement extensions versus CPU time at 200 Hz.
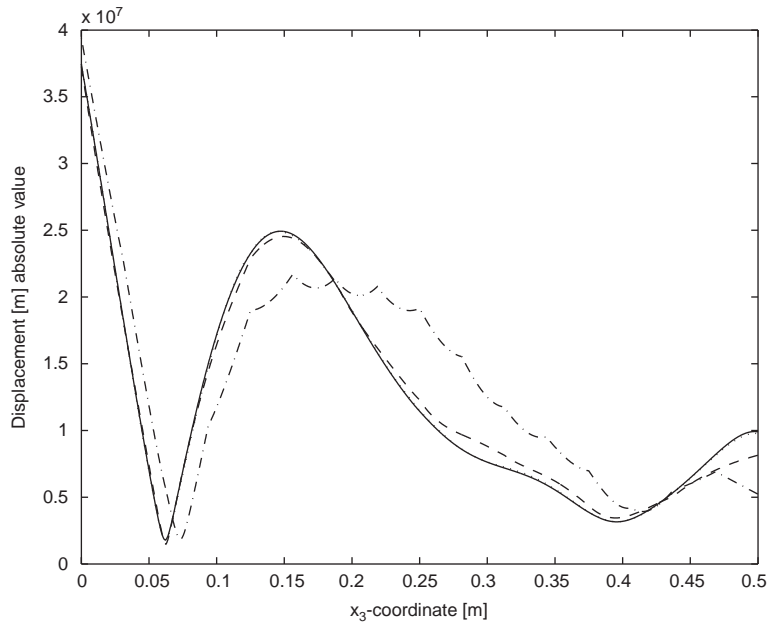

Fig. 9. u_3^s at 200 Hz: $x_1 = 0.04$ m, $x_2 = 0.06$ m. $p = 0$, $k = 16$, (dashed–dotted line); $p = 1$, $k = 8$ (dashed line); $p = 3$, $k = 4$ (dotted line); reference solution (solid line).

volume porosities are $\phi_1 = 0.98$ and $\phi_2 = 0.7$. All other material properties are identical to the previous example. On the free cross-sectional surface of layer 1, i.e., at $x_3 = 0$, a uniform normal structural traction vector is prescribed. On all other boundaries, homogeneous Neumann conditions are assumed. The porous layers, having unjacketed interfaces, are bonded to each other (cf. Section 4 and Eq. (25)).

The simulations are performed at 100 Hz for two different values of the static flow resistivity: first $\sigma = 3.75 \times 10^3$ kg/m^3 s (the same value as in previous example) and then $\sigma = 3.75 \times 10^4$ kg/m^{3}s to illustrate how the convergence rate of the fluid displacement is affected when the viscous drag increases. (Note that the viscous drag coefficient b is linearly proportional to the static flow resistivity.) In the following, the mesh size parameter k denotes the number of elements in each coordinate direction for each porous layer, i.e., the total number of elements is $2k^3$.

7.2. Result and discussion

The first case with low flow resistivity is shown in Figs. 11–13. In Fig. 11, a local behaviour close to the interface between the layers may be observed, especially close to the corner in the lower left part of the figure. It should be kept in mind that at the free side boundaries the fluid pressure is zero and thus the fluid displacement divergence is close to zero in the vicinity of those boundaries. Comparison between the fluid displacement and the solid displacement reveals an interesting difference in the convergence. As the mesh is refined, a much slower convergence may be observed for the fluid displacement in the 3-direction in Fig. 12, compared to the corresponding solid displacement in Fig. 13. Here, $p = 4$ elements were used. It should be noted that linear elements have too poor performance in this context to be practically useful, as can be seen in Fig. 14.
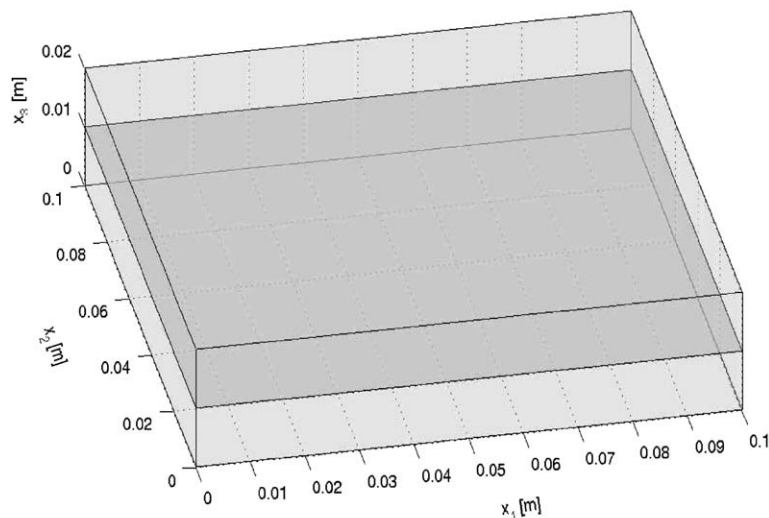

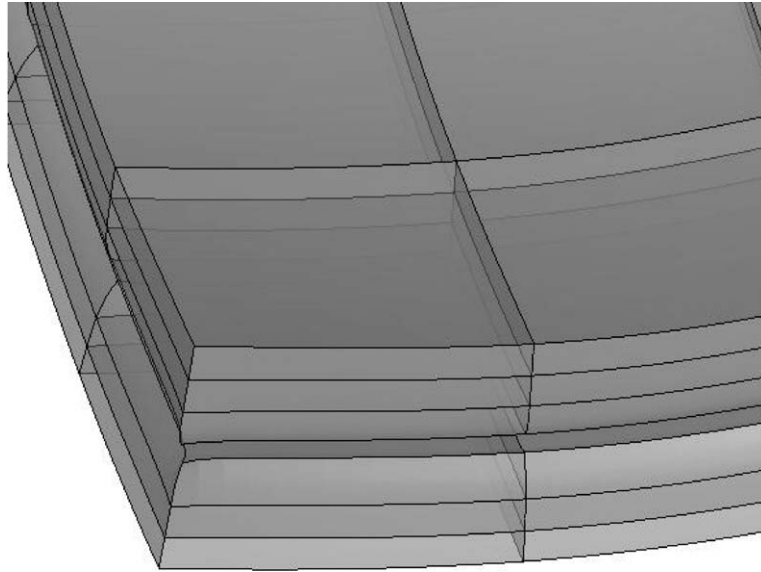Fig. 10. Sketch of the two-layered example.

Fig. 11. Deformation plot of the fluid displacement magnified with a factor of 15,000. The lower layer (layer 1) is excited on the lower (hidden) surface in upward direction. The mesh size is $3 \times 3 \times 3$ elements in each layer, $p = 6$, $\sigma = 3.75 \times 10^3 \, \text{kg/m}^3 \, \text{s}$.
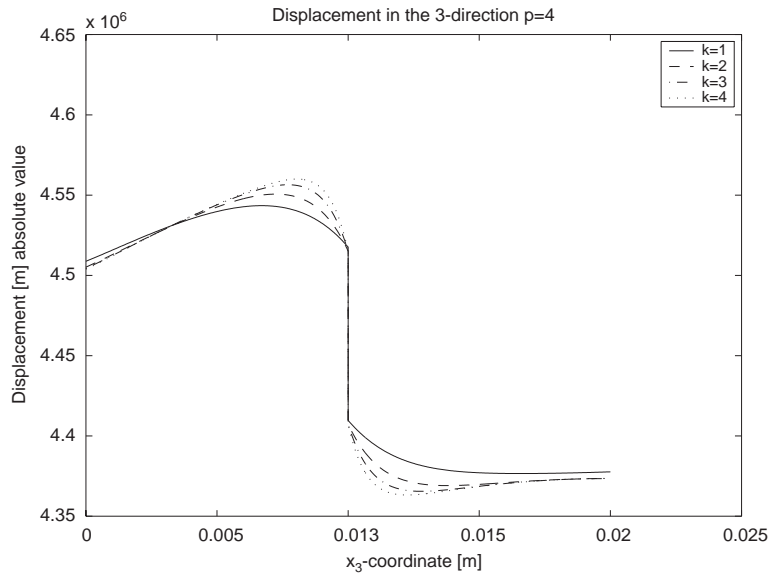

Fig. 12. u_3^f along the edge: $x_1 = 0, x_2 = 0, p = 4$; $k = 1, 2, 3, 4$ corresponding to 4896, 30,976, 96,256, 218,736 real-valued dofs.

When the flow resistivity is increased, this convergence behaviour is modified. For the case with 10 times higher static fluid resistivity, the convergence rates of the fluid displacement and the solid displacement are quite similar to each other, as can be seen in Fig. 15. The convergence behaviour
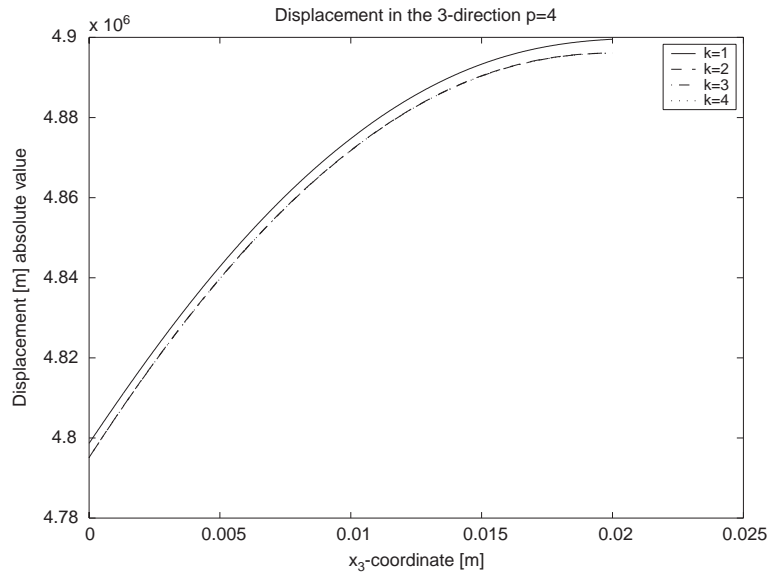
Displacement in the 3-direction p=4

Fig. 13. u_3^s along the edge $x_1 = 0, x_2 = 0$, $p = 4$; $k = 1, 2, 3, 4$.
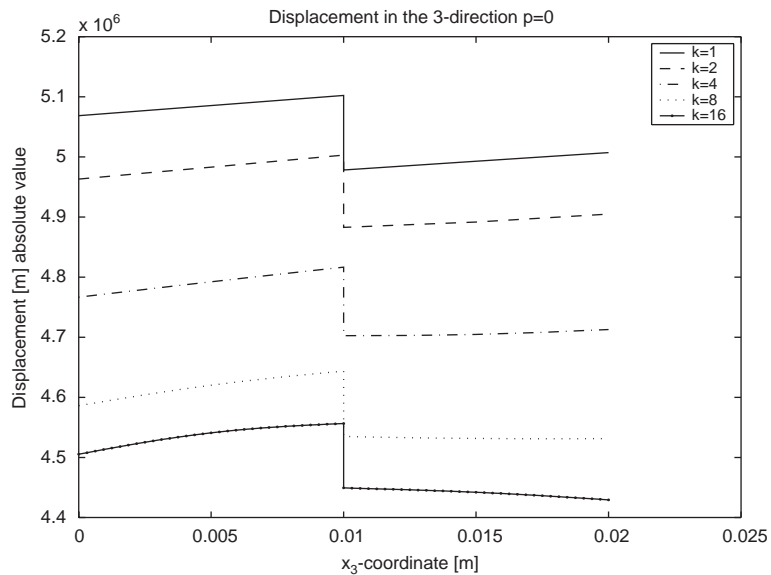
Displacement in the 3-direction p=0

Fig. 14. u_3^f along the edge $x_1 = 0, x_2 = 0$, $p = 0$; $k = 1, 2, 4, 8, 16$ corresponding to 144, 540, 2700, 16,524, 114,444 real-valued dofs.

in the former case cannot be fully explained at present, but a hypothesis is as follows: The deviatoric fluid deformation is induced by the porous frame, but the fluid has no deviatoric stiffness. Thus, this deformation is only limited by the dynamic coupling between the fluid and the
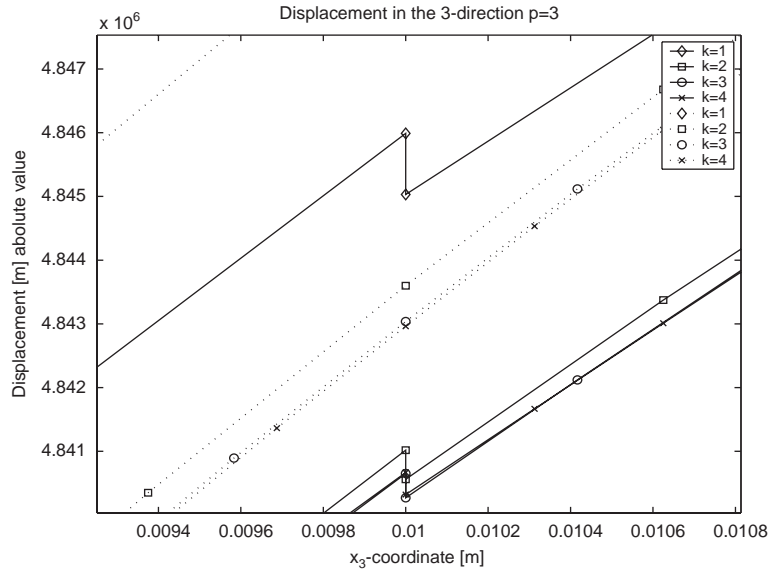
Fig. 15. u_3^s (dotted line), u_3^f (solid line) along the edge $x_1 = 0, x_2 = 0$ close to the layer interface, $p = 3$; $k = 1, 2, 3, 4$.

frame. When these couplings are weak as in the case of low static flow resistivity and a tortuosity close to unity, the fluid is less restricted by the frame and complex near-field behaviour close to material discontinuities may occur. This explanation is also supported by the fact that the convergence rate is increased when the static flow resistivity is increased. It, however, needs further investigations to be fully justified.

8. Conclusions

The hierarchical finite element formulation of Biot's equation regarding one single element presented in Ref. [4] has been extended to meshes of elements. It is proposed to apply a decomposition of the Neumann condition of the porous frame into two parts: one, containing a purely structural contribution; the other, a purely fluid pressure contribution. This decomposition is consistent with the Biot theory.

It has been pointed out that additional constraint equations are needed in order to handle discontinuities of the fluid displacement due to discontinuities in the material properties. The *hp*-convergence has been studied for a numerical example with homogeneous material properties. Mesh refinement extensions of $p = 3$ or 4 (i.e., fourth- or fifth-order polynomial finite element interpolations) were found to be the most computationally efficient in an interval of accuracy, which is interesting from an engineering application point of view.

A numerical example of a layered material with low static flow resistivity is given, showing complex fluid displacement behaviour and slow local convergence close to the intersection between free boundaries and a volume porosity discontinuity surface. This slow convergence disappears when the flow resistivity is increased.

References

[1] M.A. Biot, Theory of propagation of elastic waves in a fluid-saturated porous solid—part I. Low-frequency range, *Journal of the Acoustical Society of America* 28 (1956) 168–178.

[2] N. Dauchez, S. Sahraoui, Convergence of poroelastic finite elements based on Biot displacement formulation, *Journal of the Acoustical Society of America* 109 (1) (2001).

[3] S. Rigobert, N. Atalla, F.C. Sgard, Investigation of the convergence of the mixed displacement–pressure formulation for three-dimensional poroelastic materials using hierarchical elements, *Journal of the Acoustical Society of America* 1014 (5) (2003).

[4] N.-E. Hörlin, M. Nordström, P. Göransson, A 3-D hierarchical FE formulation of Biot's equations for elasto-acoustic modeling of porous media, *Journal of Sound and Vibration* 245 (4) (2001) 633–652.

[5] F. Ihlenburg, *Finite Element Analysis of Acoustic Scattering*, Springer, Berlin, 1998.

[6] J.-F. Allard, *Propagation of Sound in Porous Media: Modelling Sound Absorbing Materials*, Elsevier, Amsterdam, 1993.

[7] K. Dovstam, Augmented Hooke's law in frequency domain. A three dimensional material damping formulation, *International Journal of Solids and Structures* 32 (19) (1995) 2835–2852.

[8] K. Dovstam, Receptance model based on isotropic damping functions and elastic displacement modes, *International Journal of Solids and Structures* 34 (21) (1997) 2733–2754.

[9] N. Atalla, R. Panneton, P. Debergue, A mixed displacement–pressure formulation for poroelastic materials, *Journal of the Acoustical Society of America* 104 (3) (Part 1) (1998).

[10] P. Göransson, A 3-D symmetric, finite element formulation of the Biot equations with application to acoustic wave propagation through an elastic porous medium, *International Journal for Numerical Methods and Engineering* 41 (1998) 167–192.

[11] A. Houmat, Hierarchical finite element analysis of the vibration of membranes, *Journal of Sound and Vibration* 201 (4) (1997) 465–472.

[12] S.-C. Chang, T.-W. Lin, Constraint relation implementation for finite element analysis from an element basis, *Advances in Engineering Software* 10(4) 191–194.

[13] B.A. Szabó, I. Babuška, *Finite Element Analysis*, Wiley-Interscience, Newyork, 1991.